Tailoring metal-insulator transitions and band topology via off-resonant periodic drive in an interacting triangular lattice

Sayan Jana[1,2,*] Priyanka Mohan[3,†] Arijit Saha,[1,2,‡] and Anamitra Mukherjee[4,§]

[1]*Institute of Physics, Sachivalaya Marg, Bhubaneswar-751005, India*

[2]*Homi Bhabha National Institute, Training School Complex, Anushakti Nagar, Mumbai 400085, India*

[3]*Department of Theoretical Physics, Tata Institute of Fundamental Research, Homi Bhabha Road, Mumbai 400005, India*

[4]*School of Physical Sciences, National Institute of Science Education and Research, HBNI, Jatni 752050, India*

(Received 9 December 2019; accepted 11 March 2020; published 27 March 2020)

A triangular lattice with onsite Coulomb interaction U present only on one sublattice is periodically driven by electromagnetic field with a frequency $\Omega \gg (t, U)$ at half filling. In this high frequency limit, the electromagnetic vector potential, with an amplitude A, modifies the bare hopping and generates new next nearest neighbor hopping parameters. For $U = 0$, the driving acts like an emergent intrinsic spin-orbit coupling term and stabilizes three dispersive bands with the lower and upper bands having nonzero Chern numbers. Within a slave rotor mean field theory, we show that while U freezes out charge fluctuations on the interacting sublattice, it does not open up a charge gap without the external drive. In the presence of the drive, and small U, the system exhibits repeated metal-insulator transitions as a function of the amplitude A. For large U, we establish that the freezing of charge fluctuations on the interacting sublattice stabilizes an emergent, low energy *half filled noninteracting Kane-Mele model*, whose band gaps can be tuned by varying A. In this limit, we show that the external drive provides a handle to engineer periodic band inversions at specific values of A accompanied by topological phase transitions that are characterized by swapping of band Chern numbers.

DOI: 10.1103/PhysRevB.101.115428

I. INTRODUCTION

In the last decade, the advent of topological insulators (TIs) has caused a revolutionary impact on the concept of band structure of materials, both on the theoretical [1–14] as well as on the experimental [15–19] front. This has lead to intense theoretical [20–26] as well as experimental [27–29] investigation of the effects of strong correlation in systems that host nontrivial topological bands. Very recently, there has been an upsurge of research activity in emergent topological phases in *out of equilibrium* nontopological systems via external periodic driving [30–32]. Experimental feasibility of engineering such periodically driven systems [33–36] has opened up the opportunity for investigating existence of nonequilibrium Majorana modes [37–39], nontrivial transport properties [40–42], as well as controlling of band structure [43,44], disorder effect [45]. The effects of drive on the tight binding band structure in graphene [46,47], spin-orbit coupled Dirac materials like silicene and germanene [48–51], and low energy spectrum of semi-Dirac materials [52,53] are being actively pursued.

Given this background, it is natural to investigate the interplay between strong local electronic correlations and external electromagnetic driving on different model systems. This is a rather broad question and some aspects have been addressed in recent literature. There are three regimes where different theoretical tools can be applied: small driving frequency $\hbar\Omega \ll U$, near resonance $\hbar\Omega \sim U$, and off resonance $\hbar\Omega \gg U$. Dynamical localization has been investigated in one-dimensional spin half Fermi systems [54] within small frequency approximation. Effective spin model for one and two orbital Hubbard model at half filling has been studied [55]. The effect of near and off resonant driving on the double occupation in the Mott state has been investigated [56]. Also perturbative analysis of driving on Kondo insulators [57,58] has been undertaken. The Bose Hubbard model has been studied in the off resonant (high frequency) regime both experimentally [59] and theoretically [60–62].

While these have added valuable insights to the physics of driven systems, explicit study of metal-insulator transition (MIT) under driving, for Fermi systems, has not yet been addressed. Even more unexplored is the nature of MIT, when the underlying bands are driven into a topologically nontrivial regime. Here we investigate these issues for a triangular lattice with diluted Hubbard interaction at half filling. One of the concerns of periodic driving of an isolated many body system is that it leads to a featureless thermal state in long time limit [58]. However, it has been shown that the time scale of heating is exponentially/quasiexponentially slow [63–65] allowing one to work in a pre-thermal regime which survives for experimentally relevant time scales [66]. With this justification in our study we incorporate the drive via Peierls's substitution to the bare tight binding hopping through a time dependent vector potential $\mathcal{A}(t) = \{A_x \cos \Omega t, A_y \cos(\Omega t - \phi)\}$. We denote

*sayan@iopb.res.in

†priyankamohan@theory.tifr.res.in

‡arijit@iopb.res.in

§anamitra@niser.ac.in

the amplitude of the vector potential by A. We employ high frequency Brillouin-Wigner perturbation theory [67] to obtain a quasistatic effective Hamiltonian (H_{eff}) in the zero photon subspace up to the order of $1/\Omega$. The effect of driving gives rise to correction to the nearest neighbor (NN) bare hopping elements between different sublattices as well as generates new next-nearest neighbor (NNN) hopping terms [68]. These emergent hopping amplitudes are chiral in nature and act like intrinsic spin-orbit coupling, which leads to topologically nontrivial bands in the Floquet quasienergy spectrum [69]. While magnetism is certainly an important feature of the Hubbard model, here our focus lies in the study of the effect of drive only on charge fluctuations. Hence, we study our model in the paramagnetic regime within a slave rotor mean field theory (SR-MFT) [70,71].

In the uncorrelated model with three dispersive bands, nonzero A generates chiral NNN hopping terms and also modifies the bare hopping elements. The resulting Hamiltonian hosts topologically nontrivial lower and upper bands and a trivial dispersive middle band. Variation of A causes periodic touching of the three bands. Switching on U on one sublattice (on one site of the three site unit cell of the triangular lattice), induces a 'local Mott transition' beyond a threshold value of the correlation strength U_{Crit} that suppresses charge fluctuations at the correlated sublattice. In the presence of the drive, and for $U > U_{\text{Crit}}$, we show that the local Mott transition, the drive modulated NN hopping, and the emergent NNN hopping terms conspire to stabilize an insulating state. This insulating state is characterized by topologically nontrivial low energy bands split by a small charge gap and high energy bands separated by U. We show that, similar to the $U = 0$ case, the charge gap between the low energy bands oscillates periodically with A and stabilizes a semimetal at specific values of A where the charge gap goes to zero. Moreover at each such band touching there is a topological phase transition whereby the Chern number of the topologically nontrivial bands is exchanged. For a range of bare hopping parameters, we establish that this periodic gap closing and swapping of Chern numbers holds for the entire insulating regime and is independent of U, once $U > U_{\text{Crit}}$. We establish that this phenomenology can be understood in terms of an emergent low energy Hamiltonian that resembles *the half filled noninteracting Kane-Mele model*. Further, based on single particle density of states, we map out U_{Crit} as a function of A and present the U vs A phase diagram, emphasizing how the peaks and dips of U_{Crit} are governed by a competition between the interaction strength and the drive induced bandwidth modulations.

The remainder of the paper is organized as follows. In Sec. II we discuss our model, the slave rotor mean-field theory, and the observables. In Sec. III we present our numerical results. Finally, we summarize and conclude the paper in Sec. IV.

II. MODEL AND METHOD

We consider a triangular lattice as our model system with a, b, and c sublattices as shown in Fig. 1(a). The Hamiltonian of the system is defined as $H = H_{\text{Free}} + H_{\text{Int}}$. The tight binding

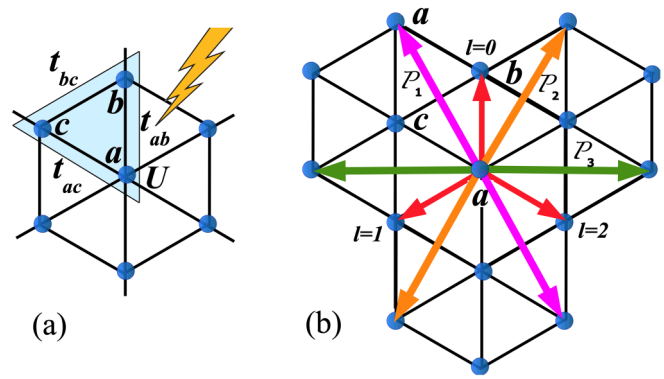

FIG. 1. (a) Schematic structure of the triangular lattice is demonstrated. Each unit cell consists of three atoms a, b, and c shown enclosed in a triangle. Here, t_{ab}, t_{bc}, t_{ca} represent the nearest neighbor hopping amplitudes between the three atoms. U denotes the strength of onsite Hubbard interaction on the a sublattice. The lightning bolt represents the external electromagnetic radiation. (b) The thin red arrows indicate the three directional vectors $l = 0, 1, 2$ in the triangular lattice. The thick, magenta, orange, and green arrows denote the light induced next nearest neighbor hopping along the path-1($\mathcal{P}_1$), path-2($\mathcal{P}_2$), and path-3($\mathcal{P}_3$), respectively, within a sublattice. Similar terms also exist for both b and c sublattices. The chirality of light induced hopping terms are discussed in the text.

Hamiltonian H_{Free} can be written as

$$H_{\text{Free}} = H_{ab} + H_{bc} + H_{ac} = -\sum_{\langle i,j\rangle}(t_{ab}a_i^\dagger b_j + t_{bc}b_i^\dagger c_j + t_{ca}a_i^\dagger c_j + \text{H.c.}), \quad (1)$$

where, t_{ab}, t_{bc}, and t_{ac} represent the nearest-neighbor (NN) hopping amplitudes between the a, b, and c sublattices. Here $a_i^\dagger(a_i)$, $b_i^\dagger(b_i)$, and $c_i^\dagger(c_i)$ correspond to the creation (annihilation) operators for the a, b, and c sublattices, respectively. For notational clarity, the spin indices are suppressed for now. The main steps here consist of first treating the effect of driving on the H_{Free} and then studying the effect of interaction on the emergent tight binding model. This is the standard procedure in the high frequency limit [56].

A. The effective kinetic energy Hamiltonian

In our analysis, we consider the high-frequency limit of the periodic driving. In this limit, one can derive an effective quasistatic Hamiltonian taking into account only the virtual photon transitions. Technically, the full Floquet Hamiltonian in the extended Sambe space is projected back to the zero photon subspace using a high-frequency expansion based on the Brillouin-Wigner (BW) perturbation theory [72]. In comparison to Floquet-Magnus [73,74] and van Vleck expansions [75,76], higher order terms are easier to calculate using BW expansion.

The vector potential of the electromagnetic radiation is given by

$$\mathcal{A}(t) = (A_x \cos\Omega t, A_y \cos(\Omega t - \phi)), \quad (2)$$

where Ω is the frequency of the light, A_x, A_y are the amplitudes of the irradiation, and ϕ is the phase. The polarization of

the laser can be controlled by choosing appropriate values for A_x/A_y and ϕ. For, e.g., circular polarization can be obtained by choosing $A_x = A_y$, $\phi = \pi/2$ and linear polarization by $\phi = 0$, respectively. The other values of A_x/A_y and ϕ correspond to elliptical polarized light.

The vector potential of the external irradiation is incorporated by Peierls substitution thereby transforming the above Hamiltonian time dependent. The hopping elements thus acquire a phase given by

$$t \to t e^{-i(r_1 \sin \Omega t + r_2 \cos \Omega t)}, \tag{3}$$

where $r_1(l) = \tilde{a} A_y \sin(\phi) \cos(\frac{2\pi l}{3})$ and $r_2(l) = \tilde{a}[A_y \cos(\phi) \cos(\frac{2\pi l}{3}) - A_x \sin(\frac{2\pi l}{3})]$. Here $l = 0, 1, 2$ denotes the three directions within the lattice as shown in Fig. 1(b) and $\tilde{a}$ is the lattice spacing.

The Floquet Hamiltonian [43,77] can be defined in the following way:

$$H^p = \frac{1}{T} \int_0^T H(t) e^{ip\Omega t} dt. \tag{4}$$

As discussed in Appendix A, the final form of the Floquet Hamiltonian is

$$H_K = H^0 + \sum_{n \neq 0} \frac{H^{-n} H^n}{n\Omega}. \tag{5}$$

For the triangular lattice under our consideration [see Fig. 1(a)], the zeroth order term is given by,

$$H^0 = -\sum_{\langle ij \rangle} J_0\left(\sqrt{r_1^2 + r_2^2}\right) \times (t_{ab}\, a_i^\dagger b_j + t_{bc}\, b_i^\dagger c_j + t_{ca}\, a_i^\dagger c_j + \text{H.c.}). \tag{6}$$

In the zeroth order Hamiltonian, the effects due to periodic driving are manifested in renormalized hopping parameters. The first order term from Eq. (5) results in an effective spin-orbit coupling as described later. Similar terms has also been reported earlier in case of hexagonal lattice (graphene) [72], spin-orbit coupled Dirac materials [51]. In our case, the $O(t^2/\Omega)$ term is shown in Eq. (7).

In Eq. (7), $\nu_{ij} = \pm 1$ depending on whether the next nearest neighbor (NNN) hopping takes place in clockwise or anticlockwise manner. This introduces an intrinsic chirality in the model, similar to intrinsic spin orbit coupling [1]. In Fig. 1(b), this external light induced spin-orbit coupling terms are denoted by paths $\mathcal{P}_1$, $\mathcal{P}_2$, and $\mathcal{P}_3$ within the a sublattice. Similar terms are also present for b and c sublattices which can be seen from Eq. (7). The full analytical form of $\chi_{1,2,3}$ in Eq. (7) is provided in Appendix A, where it is shown that for circularly polarized light, $\chi_1 = \chi_2 = \chi_3$. Also, from Eq. (7) it is apparent that for $t_{ab} = t_{bc} = t_{ca}$, the $1/\Omega$ order term vanishes.

$$\begin{aligned}\frac{H^{-n} H^n}{n\Omega} = &\sum_{\langle\langle ij \rangle\rangle}^{\mathcal{P}_1} \chi_1\, \nu_{ij} \left[\left(t_{ab}^2 - t_{ca}^2\right) a_i^\dagger a_j + \left(t_{ab}^2 - t_{bc}^2\right) b_i^\dagger b_j \right. \\ &\left. + \left(t_{ac}^2 - t_{bc}^2\right) c_i^\dagger c_j \right] \\ &+ \sum_{\langle\langle ij \rangle\rangle}^{\mathcal{P}_2} \chi_2\, \nu_{ij} \left[\left(t_{ab}^2 - t_{ca}^2\right) a_i^\dagger a_j + \left(t_{ab}^2 - t_{bc}^2\right) b_i^\dagger b_j \right. \\ &\left. + \left(t_{ac}^2 - t_{bc}^2\right) c_i^\dagger c_j \right] \\ &+ \sum_{\langle\langle ij \rangle\rangle}^{\mathcal{P}_3} \chi_3\, \nu_{ij} \left[\left(t_{ab}^2 - t_{ca}^2\right) a_i^\dagger a_j + \left(t_{ab}^2 - t_{bc}^2\right) b_i^\dagger b_j \right. \\ &\left. + \left(t_{ac}^2 - t_{bc}^2\right) c_i^\dagger c_j \right]. \end{aligned} \tag{7}$$

This is different from honeycomb lattices where the light induced spin-orbit term is nonzero irrespective of the polarization of the external irradiation [72]. In triangular lattices, the spin-orbit coupling term between each pair of next-neighbor sites has two contributions with opposite chirality. Thus, they can nullify each other if the hopping amplitudes are equal to each other. Here, we define the light induced NNN hopping amplitudes as $t_{aa} = \chi_1 \nu_{ij}(t_{ab}^2 - t_{ca}^2)$, $t_{bb} = \chi_2 \nu_{ij}(t_{ab}^2 - t_{bc}^2)$, $t_{cc} = \chi_3 \nu_{ij}(t_{ac}^2 - t_{bc}^2)$.

B. Interaction effects

To discuss the effects of H_{Int}, we first rewrite H_K is a succinct notation as a tight binding model on a triangular lattice with nearest and chiral NNN hopping and also make the spin indices explicit. The unit cell consists of three atoms indicated by a, b, and c as shown in Fig. 1(a). Hence, the kinetic term (H_K) in a compact form can be written as

$$H_K = \sum_{I,J,\alpha,\beta,\sigma} \left(t^A_{I\alpha\sigma;J\beta\sigma} d^\dagger_{I\alpha\sigma} d_{J\beta\sigma} + \text{H.c.}\right), \tag{8}$$

where the indices I, J denote the three site unit cells of the lattice. The hopping terms depend on the strength A of the external periodic drive. Here, I equal to J implies the hopping within a unit cell, while $I \neq J$ indicates to the hopping between different unit cells, while α and β runs over the three atomic labels a, b, and c. $t^A_{I\alpha\sigma;J\beta\sigma}$ parameters are appropriately chosen to incorporate NN and NNN hopping elements as necessary. The Hubbard interaction is introduced only on the a sublattice. The final form of the off-resonant Hamiltonian [68] reads as:

$$\begin{aligned} H^{\text{OR}}_{\text{eff}} = &\sum_{I,J,\alpha,\beta,\sigma} \left(t^A_{I\alpha\sigma;J\beta\sigma} d^\dagger_{I\alpha\sigma} d_{J\beta\sigma} + \text{H.c.}\right) \\ &+ \sum_I U n_{Ia\uparrow} n_{Ia\downarrow}. \end{aligned} \tag{9}$$

As is usual in slave-rotor decomposition, we rewrite the creation and annihilation operators on the site with interaction as:

$$\begin{aligned} d^\dagger_{I a\sigma} &= f^\dagger_{I a\sigma} e^{-i\theta_{Ia}}, \\ d_{I a\sigma} &= f_{I a\sigma} e^{i\theta_{Ia}}. \end{aligned} \tag{10}$$

Here $f^\dagger_{Ia\sigma}$ is the spinon operator at the a site in the Ith unit cell and $e^{\pm i\theta_{ia}}$ denotes the rotor creation and annihilation operators defined through its action as follows: $e^{\pm i\theta_{I\alpha}} |n^\theta_{I\alpha}\rangle = |n^\theta_{I\alpha} \pm 1\rangle$. At half filling, to preserve the physical Hilbert space on the interacting site we impose the following operator constraint:

$$\left(n^\theta_{Ia} + n^f_{Ia\uparrow} + n^f_{Ia\downarrow}\right) = 1, \tag{11}$$

with electron occupation equal to that of the spinon, i.e., $n^f_{I a\sigma} = n^e_{I a\sigma}$, where $n^f_{I a\sigma} = f^\dagger_{I a\sigma} f_{I a\sigma}$. We now treat $H^{\text{OR}}_{\text{eff}}$ within a mean field scheme. We refer the reader to literature for the

details of the slave rotor mean field method [70,71]. Here we briefly outline the method in the context of our calculations. We make a mean field ansatz for the many body ground state [69] as $|\Psi\rangle = |\Psi^{fd}\rangle|\Psi^{\theta}\rangle$, where the superscript d refers to a collective index representing the operators on the b, c sublattices, the spinon operator on the a sublattice is denoted by the f and the rotor operator by θ superscript. We note that, considering Hubbard interaction U only on single site is rather interesting as there is spinon contribution emerging from the a site and the free electron contribution from the b, c sites. This type of mixed quasiparticle contribution in the topological edge modes is novel in nature [26]. Also this gives rise to correlated metallic behavior as seen in the total density of states of the system [26]. Moreover, the scenario of large U on one sublattice and $U = 0$ or very small on the other sublattices is not novel but routinely occurs in strongly correlated materials (for, e.g., CuO_2, $LaNiO_3$, etc.) [78,79]. The next step is to compute the expectation values $H_{fd} \equiv \langle\Psi^{\theta}|H|\Psi^{\theta}\rangle$ and $H_{\theta} \equiv \langle\Psi^{fd}|H|\Psi^{fd}\rangle$ which are solved self consistently all the while respecting the above constraint at a mean field level by suitable introductions of chemical potentials. The full detailed expressions are provided in Appendix B. Here we note that H_{θ} is the interacting problem that is solved with a cluster mean field theory. For the choice of the hopping amplitudes discussed below, we use a single site rotor cluster, containing one a site, for our results. We have contrasted the results against the solution of bigger clusters containing two interacting a sites as well. We now describe the observables calculated before proceeding to the results.

C. Observables

Within the SR-MFT, the first important indicator is $\langle\Psi^{\theta}|e^{-i\theta_{Ia}}|\Psi^{\theta}\rangle \equiv \Phi_{Ia}$ and it is assumed to be uniform or site independent. When $\Phi_{Ia} = 0$ charge fluctuations on the a sites are suppressed [70,71]. This signals a 'local' Mott transition. However, with U operative only on the a sublattice, *this does not guarantee an insulating ground state*. For the metal-insulator transitions, we rely on the sublattice projected density of states (PDOS) defined as $N_{\gamma}(\omega) = \sum_{\alpha,\sigma}\sum_{i_{\gamma}}|\langle\chi_{\alpha}|i_{\gamma},\sigma\rangle|^2\delta(\omega-\epsilon_{\alpha})$, where, $\gamma = a, b, c$ sites in the Ith unit cell. Here, $\{|\chi_{\alpha}\rangle\}$ and $\{\epsilon_{\alpha}\}$ correspond to the eigenvectors and eigenvalues of $H_{\rm eff}^{\rm OR}$. The derivation is straightforward and is provided in Appendix B. We also compute the Chern number for the bands and the edge modes in the strip geometry for H_{fd}, which provides information on the electron-spinon band topology. There are standard methods to investigate them which are discussed in Appendix C. For H_{θ} with more than one a site, as illustrated in Appendix D, we also have to calculate $\langle\Psi^{\theta}|e^{-i\theta_{Ia}}e^{i\theta_{Ja}}|\Psi^{\theta}\rangle$, which encodes rotor kinetic energy within the enlarged cluster. In the insulating regime, this plays the role of virtual charge fluctuations between the a sites in the rotor cluster, even if $\Phi_{Ia} = \Phi_{Ja} = 0$. This will be elaborated on more later in the paper.

III. RESULTS

In this section, we present our results for the band spectrum, order parameter, and total density of states (DOS). Throughout our analysis, we have chosen $\Omega = 10t \gg (t, U)$ to be in the high frequency regime and $A_x = A_y = \zeta$, $\phi = \pi/2$, i.e., circularly polarized light as our external electromagnetic drive. We denote the amplitude of the vector potential, for this choice by $A \equiv \sqrt{2}\zeta$. All energies are measured in units of the nonirradiated ($A = 0$), bare b-c hopping parameter $t_{bc} \equiv t$, which is chosen to be 1. In these units, we choose $t_{ac} = t_{ab} = 0.5t$. From Eq. (7) we find that for this choice only b-b and c-c NNN hoppings survive in the $1/\Omega$ order term of $H_{\rm eff}^{\rm OR}$. Furthermore, the emergent t_{bb} is always equal to t_{cc}. Initially we will focus on results for these choices of parameters, we will then discuss effects on nonzero t_{aa} achieved by setting $t_{ab} \neq t_{ac}$. We also use a dimensionless parameter A/t to quantify the magnitude of the vector potential, which is equivalent to measuring the magnetic vector potential in [Ampere $\times$ meter]$^{-1}$.

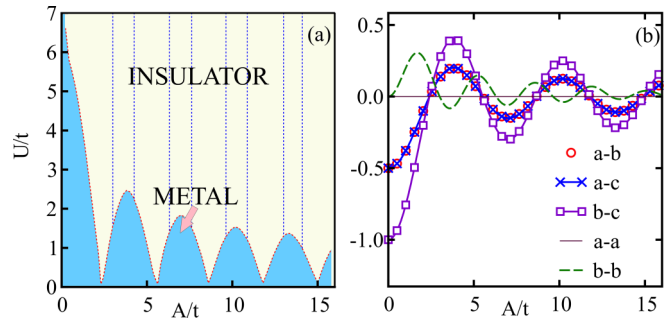

FIG. 2. The U-A phase diagram is shown in panel (a). The red (dashed) line with squares depicts the evolution of $U_{\rm Crit}$ with A/t. The region below $U_{\rm Crit}$ is metallic and above $U_{\rm Crit}$ is insulating except at special values of A/t, indicated by vertical (dashed) blue lines. At these values of A/t, bands of the insulating state touch, leading to a semimetallic behavior. Panel (b) shows the dependence of the NN and NNN hopping parameters of the triangular lattice as a function of the driving amplitude A/t. The NNN hopping amplitudes (t_{bb}, t_{cc}) are small, so for visual clarity, they are magnified by a factor of 16. In the case shown here, NNN hopping parameter t_{aa} is explicitly chosen to be zero as $t_{ab} = t_{ac} = 0.5t$.

Figure 2 shows the U-A phase diagram at zero temperature and summarizes the main results for $t_{ac} = t_{ab} = 0.5t$. In panel (b), we plot the variation of the NN and the NNN hopping amplitudes as a function of the radiation amplitude. We begin with the two limiting cases, i.e., only A and only U, before discussing their combined effects shown in Fig. 2(a).

A. Noninteracting driven system

For $A = U = 0$, the system consists of three dispersive bands, which touch at specific momenta points in the Brillouin zone. The bands are shown in Fig. 3(a). From Fig. 2(b) we find that the NN hopping amplitudes oscillate with a decaying envelope with increasing A, following the Bessel function form in Eq. (6). In addition, the NNN hoping amplitudes t_{bb} and t_{cc} emerge with A and also oscillate with a decaying envelope. These oscillations are due to the A dependence of the pre-factors χ_2 and χ_3 of $t_{ab}^2 - t_{bc}^2$ and $t_{ac}^2 - t_{bc}^2$, respectively, which we define as t_{bb} and t_{cc} earlier. The expressions for χ_2 and χ_3 are given in Appendix A, Eq. (A6). We find that these oscillations cause a periodic opening and closing of band gap in the noninteracting model. Two typical cases for $A/t \sim 1.5$

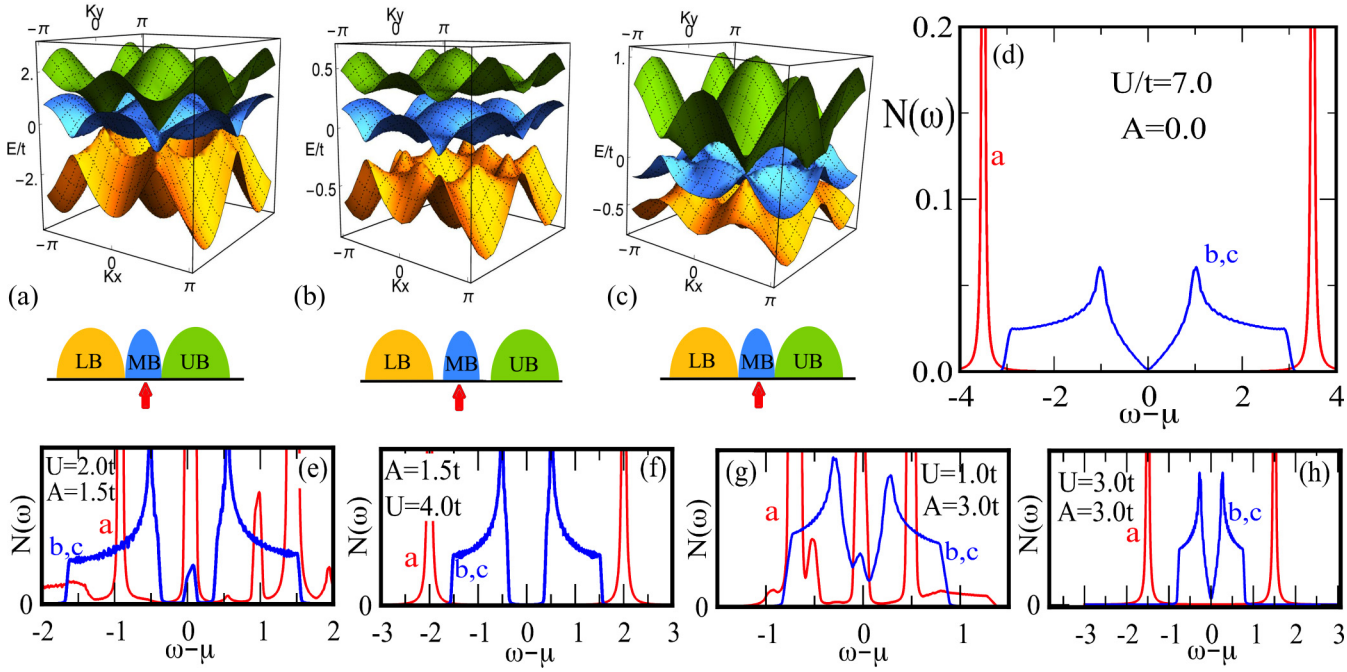

FIG. 3. Panels (a) to (c) show the noninteracting tight binding bands of driven triangular lattice. Panel (a) depicts the energy band dispersion and schematic DOS for $A = 0$, while panel (b) and (c) manifest the same for $A = 1.5t$ and $A = 3t$, respectively. In all three panels, the dispersive middle band is half filled which is shown by the small red arrow indicating the position of the chemical potential μ. The band touching points for $A = 0$ are removed and band gaps open up at $A \sim 1.5t$. The bands again touch for $A \sim 3t$. Panel (d) shows the sublattice resolved DOS for $A = 0$ and $U = 7t$. Panels (e) to (h) show the evolution of the sublattice resolved DOS with U, for fixed $A = 1.5t$ in (e) and (f) and for $A = 3t$ in (g) and (h).

and $A/t \sim 3.0$ are shown in Figs. 3(b) and 3(c). The schematic of the DOS depicting the closing and opening of the band gaps is shown directly below the bands for the three values of A in panels (a) to (c). The red arrow denotes the chemical potential for half filling. For $A/t \sim 1.5$, when the bands are separated, we find that the lowest band has a Chern number -1, the middle band is topologically trivial, and the highest band has a Chern number $+1$. From then on, beyond every A at which the bands touch, the upper and lower bands exchange their Chern indices. This shows that at half filling, the driven triangular lattice system always has a metallic ground state for $U = 0$, but with nontrivial topological energy bands.

B. Large U limit of the purely interacting system

Figure 3(d) shows the sublattice resolved PDOS for $U = 7t$ for $A = 0$. We see that large U causes a charge gap, of the order of U, in the states from the a sublattice, as seen from the red curve. At half filling, the average a site occupation, $\langle n_a \rangle$ is 1. The half filled configuration constitutes the lowest band in the a sublattice PDOS, the peak around $\omega - \mu = 4$ in panel (d). Any further occupation on the a sublattice is pushed up in energy by U. The remaining b-c sublattice forms a low energy band (blue cure) hybridizing through t_{bc}. In the large U limit, the effect of the hybridization between the b-c and the a sublattices is negligible as virtual charges are suppressed due to large U. Thus, the lattice connectivity for the low energy bands is that of a hexagon [see Fig. 1(b)] and the system shows graphenelike semimetallic behavior. From Fig. 4(d), we see that Φ_{Ia} goes to zero for $U > 5.8t$ and $A = 0$. This corroborates the PDOS by showing that the charge fluctuations are completely suppressed at large U at the a sublattice [80]. Based on the above discussion, it then implies that for $A = 0$ and $U/t > 5.8$, the low energy bands, the ones closest to the Fermi level, are predominantly constituted by electronic states delocalizing in the b-c sublattice and are a topologically trivial semimetal.

C. Interaction effects on the driven system

Figures 3(e) and 3(f) show the PDOS for $U/t = 2$ and 4, respectively, for fixed $A = 1.5t$. We see that all three sublattices contribute to the spectral weight at the Fermi energy in (e), while in (f), a finite charge gap is clearly visible. A metallic behavior is also found for small U/t (=1) for $A = 3t$ as seen in panel (g), which is similar to panel (e). However on increasing U to $3t$ while staying at $A = 3t$, as shown in panel (h), we see a semimetallic behavior, much like in the $A = 0$ case. In U-A phase diagram shown in Fig. 2(a), the entire insulating regime has a gapped DOS as in Fig. 3(f), except for special values of A (marked by the vertical blue dashed line) where the semimetallic ground state, as seen in Fig. 3(h), are located.

To understand this contrasting behavior in the insulating regime, we first note that as discussed in Sec. II, finite A/t generates NNN b-b and c-c hopping terms that are chiral in nature and thus acts as an intrinsic spin-obit coupling. Secondly, in Appendix B we also show that these NNN terms (t_{bb} and t_{cc}) are not renormalized by the interaction effects. We find that although t_{bb} and t_{cc} are small in magnitude, with a maximum possible value of $0.018t$ as seen from Fig. 2(b)

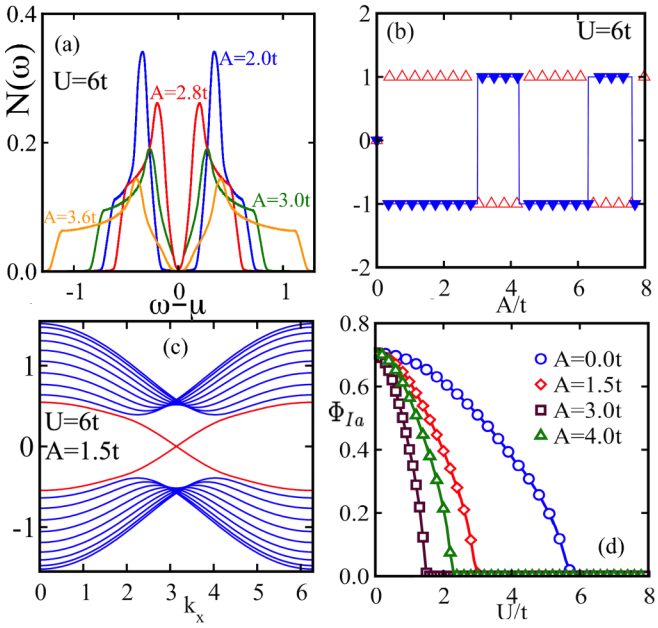

FIG. 4. In panel (a), we show the evolution of the charge gap in the low energy bands as a function of A for $U = 6t$. Panel (b) depicts the Chern numbers for the top and the bottom bands of H_{fd} as a function of A for the same $U(=6t)$, as in panel (a). Panel (c) shows the edge modes for the band calculations in strip geometry for a typical value of $A = 1.5t$ in the insulating regime ($U = 6t$). The red lines are the topologically protected zero energy edge modes. Panel (d) demonstrates the dependence of order-parameter Φ_{Ia} on U, for various values of A. The value of U for local Mott transition at the a sublattice has a nonmonotonic dependence on the driving amplitude A.

at $A = 1.7t$, they have a drastic impact on the bands of the model. Thirdly, in the insulating regime, Φ_{Ia} is always zero and any contribution from the a sublattice are far removed from the Fermi level, as also seen from the PDOS contributions from the a sublattice in Figs. 3(f) and 3(h). Thus, the low energy kinetic energy comes primarily from the t_{bc} with small contributions from NNN t_{bb} and t_{cc}. Thus, the low energy bands (close to the Fermi level) have NN hopping and chiral NNN hopping terms, which is the hopping connectivity of the noninteracting Kane-Mele model. Moreover, since the a sites have an average occupation of one electron, the emergent noninteracting Kane-Mele model is also at half filling. For a general value of A, our calculations reveal that the ground state of this low energy model hosts two distinct bands and that the band gap between these can be tuned by varying A. These low energy bands are shown in Fig. 4(a) in the insulating regime ($U = 6t$). It shows that the charge gap at $A = 2$ reduces and closes at $A = 3t$ forming a semimetal. It then opens again up immediately (data is shown for $A = 3.6t$). In addition, the chiral nature of the NNN hopping amplitudes make these low energy bands topologically nontrivial, as is expected in the Kane-Mele model.

Finally, owing to the oscillatory dependence of the hopping amplitudes on A, the gap closing discussed above occurs repeatedly for specific values of A. We compute the Chern number for the H_{fd}, after the SR-MFT convergence has been achieved. The effect of the rotor Hamiltonian is encoded in the renormalization of the a-b and a-c hopping terms as seen from Eq. (B1) in Appendix B. In Eq. (B1) we see that Φ_{Ia} multiplies both t_{ab} and t_{ac}, so in the insulating regime ($\Phi_{Ia} = 0$) these hopping paths are switched off. Thus calculating the Chern number from the remaining terms in H_{fd} suffices to calculate the topological properties of the low energy Kane-Mele model. Figure 4(b) shows this evolution of the Chern numbers, as a function of A/t for $U/t = 6$. As a function of A, the Chern numbers of the two bands are swapped periodically. We see that the Chern numbers are swapped exactly at the band touching point $A = 3t$, as seen from panel (a). In Fig. 4(c) we show the edge states computed from the eigenstates of H_{fd} on a strip geometry for a specific value of A as indicated in the caption. Details of the calculations are presented in Appendix C. We find a linearly dispersing electronic edge mode, as expected for the Kane-Mele model.

We now consider the dependence of $U_{\rm Crit}$ on A, the red (dashed) curve in Fig. 2(a). First of all, we observe an overall suppression of $U_{\rm Crit}$ with increasing A. This is because of the gradual suppression of all the hopping amplitudes with A, as seen in panel (b). We also notice that the NN hopping amplitudes oscillate *in phase* with each other. This modulation of the hopping controls the bandwidth which imprints on the A dependence of $U_{\rm Crit}$, exhibiting that a larger U is needed when the hopping amplitudes are larger. Similarly the minima of $U_{\rm Crit}$ occurs for A values where the three NN amplitudes are closest to zero, effectively narrowing the bandwidth. The value of U minima which Φ_{Ia} becomes zero also has a similar nonmonotonic behavior as seen in panel Fig. 4(d). For the range of A values shown, the smallest U for $\Phi_{Ia} = 0$ occurs for $A = 3t$. This shows that the metal-insulator transition is primarily controlled by the competition between various hopping elements and U.

D. Nonzero t_{aa} and spinon contributions

So far, we have focused on the case of $t_{ab} = t_{ac}$ for which the emergent NNN t_{aa} always remains zero and have employed a single site rotor cluster in our calculations. A single site rotor cluster cannot capture rotor kinetic energy as there is only one rotor site in H_θ. Although larger clusters are preferred, exponential growth of the rotor Hilbert space forces a compromise. We now use a cluster with four sites, containing two a sites, each connecting to a single b and another c site. The schematic is shown in Appendix D, Fig. 6(b). We have checked that when $t_{aa} = 0$, the larger cluster results agree well with the single site cluster results. This is because of the following reason.

First, so far as H_{fd} is concerned, the rotor kinetic energy $\langle\Psi^\theta|e^{-i\theta_{Ia}}e^{i\theta_{Ja}}|\Psi^\theta\rangle$ only renormalizes t_{aa} as seen from Eq. (D1) in Appendix D. In the insulating regime, even when $\Phi_{Ia} = 0$, the rotor kinetic energy term $\langle\Psi^\theta|e^{-i\theta_{Ia}}e^{i\theta_{Ja}}|\Psi^\theta\rangle$ remains finite. However, if $t_{aa} = 0$ explicitly, there is no change in the Hamiltonian H_{fd}. But H_θ now has a new kinetic term as seen in Eq. (D2) which can affect the value of $U_{\rm Crit}$. Nonetheless, particularly in the large U insulating regime, the rotor kinetic energy is suppressed, to the lowest order, by $(\sim|t^{aa}|^2/U)$, so the large U band touching are not affected. In our calculation, we find very small renormalization of $U_{\rm Crit}$,

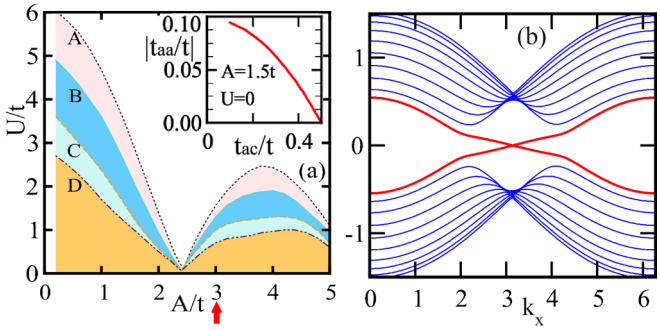

FIG. 5. In panel (a) we compare the dependence of $U_{\rm Crit}$ on A for $t_{aa} = 0$ (curve A) with that for finite NNN t_{aa}. The results are shown for fixed $t_{ab} = 0.5t$ and $t_{ac} = 0.45t$ (curve B), $0.3t$ (curve C), and $0.2t$ (curve D) which leads to small finite t_{aa}. For each $U_{\rm Crit}$ curve, the corresponding region above the curve in an insulator. The vertical red arrow denotes the first band touching value of A in the insulating regime. This location remains unchanged for all four cases shown. Inset in panel (a) shows the NNN $|t_{aa}/t|$ as a function of t_{ac} when $U = 0$ and A is fixed at $1.5t$. For this t_{ab} is kept fixed at $0.5t$ and t_{ac} is varied between $0.5t$ to $0.1t$. The hopping variation will be discussed in the text. As in Fig. 2(b), the NNN hopping amplitude t_{aa} is magnified 16 times. Panel (b) illustrates the edge modes for case B, with $U = 6t$ and $A = 1.5t$.

but there are no qualitative changes. Below we discuss the case of $t_{aa} \neq 0$, where the corrections to $U_{\rm Crit}$ are significant, but the values of A for the band touchings in the insulating regime remain unchanged within numerical accuracy.

To perform a systematic study, we have kept $t_{ab} = 0.5t$ and varied t_{ac} from $0.5t$ to $0.1t$. The resulting t_{aa}, when $U = 0$, is shown in the inset of Fig. 5(a) for $A = 1.5t$, magnified 16 times for better clarity. In Appendix D, Fig. 6(c), we compare the NNN hopping terms, for a range of A values. Although, t_{aa} is of the same order as t_{bb} and t_{cc}, as discussed above, t_{aa} is significantly suppressed in the large U insulating limit due to the heavily reduced rotor kinetic term multiplying it. Thus, the band touching locations are unchanged. The U-A phase diagram with many band touching points for the four site cluster calculations and a specific finite t_{aa} are shown in Fig. 6(a) for comparison with Fig. 2(a). This shows that the low energy Hamiltonian is, still to a very good approximation, described by a Kane-Mele model. The dispersive edge modes shown in Fig. 5(b) still maintain a linear dependence on momentum. The changes in comparison to Fig. 4(c) is due to the small rotor kinetic energy that makes the $\langle \Psi^\theta | e^{-i\theta_{Ia}} e^{i\theta_{Ja}} | \Psi^\theta \rangle \times t_{aa}$ finite. This also shows that the topologically protected edge modes now have both electron and spinon contributions. In the main panel of Fig. 5, we show $U_{\rm Crit}$ in the U-A plane for four values of t_{aa}. The curves are labeled from A to D with increasing magnitude of t_{aa}, with $t_{aa} = 0$ for curve A. We see that $U_{\rm Crit}$ is progressively suppressed as t_{aa} increases. This in simply due to increase in the bandwidth as additional electron delocalization paths are now available.

E. Experimental feasibility

Triangular lattice has been realized in ^{87}Rb, bosonic, cold atom system [81] by the application of three laser beams. Also the Fermi Hubbard model has been engineered in one dimension [82]. In this work [82] using fermionic ^{40}K atoms, intersite tunneling (hopping) amplitude is controlled by the magnitudes of the laser beams, whereas the Hubbard interaction strength can be controlled by changing the occupancy (number of atoms) in the harmonic trap. Further, for periodic driving of bosonic optical system (^{87}Rb) via sinusoidal shaking of the lattice corresponding to a time-varying linear potential has also been achieved [83]. Finally, we would like to mention how the spatial modulation of two body interaction in Fermi systems can be realized. The interaction between the fermions is proportional to the scattering length [84], among other quantities. The scattering length is in turn dependent on the coupling strength as well as the energy detuning between the scattering and the molecular channels, in the two channel model of Feshbach resonance [85]. The coupling between these two channels can be spatially modulated by employing optical Feshbach resonance technique, where counterpropagating lasers are applied on the optical lattice. The applied lasers form a spatially varying intensity profile that modulates

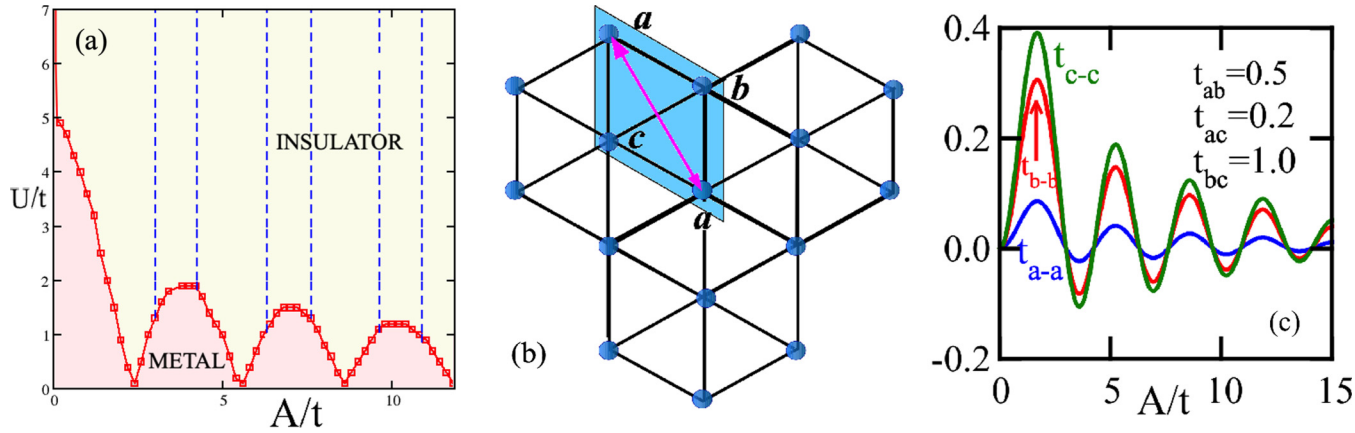

FIG. 6. U-A phase diagram for nonzero t_{aa}, when $t_{ac} = 0.45t$ and $t_{ab} = 0.5t$, is shown in panel (a). Panel (b) depicts the schematic of the lattice, where the four site cluster (shaded parallelogram) is used in the rotor calculation. The NNN hopping element t_{aa} within the cluster is shown by the magenta arrow. (c) The NNN hopping amplitudes as a function of A are shown for the chosen bare NN hopping parameters as indicated.

the interaction strength on the optical lattice. This has been achieved in Fermi systems experimentally [86] and analyzed theoretically [84].

Based on these, it is clear that the experimental techniques do exist to periodically drive a Fermi system on a triangular lattice with spatially varying interaction strength. Here we briefly mention some typical experimental parameters, gleaned from the above mentioned experiments, that would be relevant for possible realization of our results in cold atomic systems. Typical values of the Hubbard interaction (U/h) in fermionic systems studied in one dimension are in the range ∼5–10 KHz [82], where h is the Planck's constant. Also, depending upon the recoil energy and the lattice potential depth one can tune the range of nearest site tunneling from 0.1–1 KHz [81,82]. Further, for the periodically driven bosonic optical system with ^{87}Rb, it has been shown that the amplitude of the effective periodically modulated hopping $t_{\rm eff}(A,\omega)/h$ changes from 0–1 KHz [83]. Further the frequency of the drive can be within the range 20–30 KHz to be in the high frequency regime. To validate our phase diagram, the typical values of the driving strength A and interaction strength U can thus range from ≈ 1–10 KHz and ≈ 2–10 KHz, respectively, in fermionic systems such as in ^{40}K atoms. We emphasize that these parameters are merely a guide for possible experiments.

IV. SUMMARY AND CONCLUSIONS

To summarize, in this paper, we have investigated the impact of strong onsite repulsion in a periodically driven triangular lattice. Driving induces modulation of the bare hopping elements of the triangular lattice and generates chiral NNN hopping terms. In the noninteracting limit, this stabilizes a metal with topologically trivial conduction band and topologically nontrivial, filled and empty bands. Weak interactions on one sublattice, for a wide range of bare hopping parameters, leads to repeated metal-insulator transitions as a function of the amplitude of the electromagnetic vector potential. In the large interaction (insulating) regime, the ground state is characterized by widely separated bands emerging from the interacting sublattice and small charge gap bands from the rest of the noninteracting sublattice. In this limit, the low energy theory (around the Fermi level) is that of a *noninteracting Kane-Mele model that is stabilized by strong interaction effects* and is shown to host bands with nontrivial topology. We have established that tuning the amplitude of the electromagnetic vector potential can be a way to control the intrinsic spin-orbit coupling term of the emergent Kane-Mele model. This can lead to periodic band touchings that split the insulating regime by introducing semimetallic ground states, at which there are topological phase transitions characterized by swapping of band Chern numbers.

ACKNOWLEDGMENTS

We acknowledge the use of the SAMKHYA: High Performance Computing Facility provided by IOP, Bhubaneswar and NOETHER cluster at NISER, Bhubaneswar for carrying out our computational work. A.M. acknowledges useful discussions with Kush Saha, NISER, India. We also acknowledge useful inputs from Ashok Mohapatra, NISER, India

APPENDIX A: DERIVATION OF THE EFFECTIVE FLOQUET HAMILTONIAN IN BW APPROXIMATION

In this subsection we present a full derivation of the effective Hamiltonian used in Eqs. (5)–(7). We begin with the tight-binding Hamiltonian of the triangular lattice as written in Eq. (1) and irradiate it with a laser with vector potential given by $\mathcal{A}(t) = (A_x \cos\Omega t, A_y \cos(\Omega t - \phi))$. For notational clarity, in this subsection, the spin indices are suppressed. The hopping amplitudes will pick up a phase from the Peierl's substitution given by: $t \to te^{-i\mathcal{A}(t)\cdot\delta_l}$. Here δ_l is the distance between nearest neighbor sites given by, $\delta_l = \tilde{a}(\cos\theta_l, \sin\theta_l)$, with $\tilde{a}$ is the lattice spacing, $\theta_l = \frac{\pi}{2} + \frac{2\pi l}{3}, \quad l = 0, 1, 2$ as shown in Fig. 1(b). This yields

$$\mathcal{A}(t)\cdot\delta_l = \tilde{a}A_y \sin(\phi)\cos\left(\frac{2\pi l}{3}\right)\sin(\Omega t) + \tilde{a}\left(A_y\cos\phi\cos\left(\frac{2\pi l}{3}\right) - A_x\sin\left(\frac{2\pi l}{3}\right)\right)\cos\omega t. \tag{A1}$$

Using the expression $\exp(-i(r_1\sin\Omega t + r_2\cos\Omega t)) = \sum_m J_{-m}(\sqrt{r_1^2+r_2^2})\exp[im(\Omega t + \arctan(\frac{r_2}{r_1}))]$, the time dependent Hamiltonian can be written as

$$H(t) = -\sum_{\langle i,j\rangle}\sum_m J_{-m}\left(\sqrt{r_1^2+r_2^2}\right)e^{im(\Omega t+\arctan(\frac{r_2}{r_1}))}(t_{ab}\,a_i^\dagger b_j + t_{bc}\,b_i^\dagger c_j + t_{ac}\,a_i^\dagger c_j) + \text{H.c.}, \tag{A2}$$

where $r_1(l) = \tilde{a}A_y\sin\phi\cos\frac{2\pi l}{3}$, $r_2(l) = \tilde{a}(A_y\cos\phi\cos\frac{2\pi l}{3} - A_x\sin\frac{2\pi l}{3})$, and J_m is the Bessel function of order m.

The Floquet Hamiltonian is defined as

$$H^K = \int_0^T dt\, H(t)\, e^{iK\Omega t}. \tag{A3}$$

Substituting for Hamiltonian from Eq. (A2) in the above equation gives the Floquet Hamiltonian:

$$\begin{aligned} H^K = -\sum_{\langle i,j\rangle}\Big[&J_K\left(\sqrt{r_1^2+r_2^2}\right)e^{-iK\arctan(\frac{r_2}{r_1})}(t_{ab}\,a_i^\dagger b_j + t_{bc}\,b_i^\dagger c_j + t_{ac}\,c_i^\dagger a_j) \\ &+ J_{-K}\left(\sqrt{r_1^2+r_2^2}\right)e^{-iK\arctan(\frac{r_2}{r_1})}(t_{ab}\,b_i^\dagger a_j + t_{bc}\,c_i^\dagger b_j + t_{ac}\,a_i^\dagger c_j)\Big]. \end{aligned} \tag{A4}$$

In this paper, we consider a high-frequency limit where the frequency of the drive is larger than the bandwidth of the system. As mentioned in Sec. II, only virtual photon transitions are allowed in this limit. Therefore one can find an effective quasistatic Hamiltonian using one of high-frequency expansion schemes such as Brillouin-Wigner [72], Floquet-Magnus [73,74], or van Vleck [75,76]. We use the Brillouin-Wigner scheme where the effective Hamiltonian to order $O(1/\Omega)$ has the form,

$$H_K = H^0 + \sum_{n\neq 0} \frac{H^{-n}H^n}{n\Omega}.$$

The zeroth order term is given by

$$H^0 = -\sum_{\langle ij\rangle} J_0\big(\sqrt{r_1^2+r_2^2}\big)(t_{ab}\, a_i^\dagger b_j + t_{bc}\, b_i^\dagger c_j + t_{ac}\, c_i^\dagger a_j + \text{H.c.}),$$

and the $O(1/\Omega)$ terms are given by

$$\begin{aligned}\frac{H^{-n}H^n}{n\omega} = &\sum_{\langle\langle ij\rangle\rangle}^{\mathcal{P}_1} \chi_1\, v_{ij}\left((t_{ab}^2 - t_{ac}^2)a_i^\dagger a_j + (t_{ab}^2 - t_{bc}^2)b_i^\dagger b_j + (t_{ac}^2 - t_{bc}^2)c_i^\dagger c_j\right)\\ &+ \sum_{\langle\langle ij\rangle\rangle}^{\mathcal{P}_2} \chi_2\, v_{ij}\left((t_{ab}^2 - t_{ac}^2)a_i^\dagger a_j + (t_{ab}^2 - t_{bc}^2)b_i^\dagger b_j + (t_{ac}^2 - t_{bc}^2)c_i^\dagger c_j\right)\\ &+ \sum_{\langle\langle ij\rangle\rangle}^{\mathcal{P}_3} \chi_3\, v_{ij}\left((t_{ab}^2 - t_{ac}^2)a_i^\dagger a_j + (t_{ab}^2 - t_{bc}^2)b_i^\dagger b_j + (t_{ac}^2 - t_{bc}^2)c_i^\dagger c_j\right),\end{aligned} \tag{A5}$$

where

$$\begin{aligned}\chi_1 &= \frac{i}{n\omega} J_n(\tilde{a}A_y) J_n\left(\frac{\tilde{a}}{2}\sqrt{A_y^2 + 3A_x^2 + 2\sqrt{3}A_xA_y\cos\phi}\right)\sin\left(n\left[\frac{\pi}{2} - \phi - \arctan\left(\frac{A_y\cos\phi + \sqrt{3}A_x}{A_y\sin\phi}\right)\right]\right)\\ \chi_2 &= \frac{i}{n\omega} J_n(\tilde{a}A_y) J_n\left(\frac{\tilde{a}}{2}\sqrt{A_y^2 + 3A_x^2 - 2\sqrt{3}A_xA_y\cos\phi}\right)\sin\left(n\left[\frac{\pi}{2} - \phi - \arctan\left(\frac{A_y\cos\phi - \sqrt{3}A_x}{A_y\sin\phi}\right)\right]\right)\\ \chi_3 &= \frac{i}{n\omega} J_n\left(\frac{\tilde{a}}{2}\sqrt{A_y^2 + 3A_x^2 + 2\sqrt{3}A_xA_y\cos\phi}\right) J_n\left(\frac{\tilde{a}}{2}\sqrt{A_y^2 + 3A_x^2 - 2\sqrt{3}A_xA_y\cos\phi}\right)\\ &\quad\times \sin\left(n\left[\arctan\left(\frac{A_y\cos\phi + \sqrt{3}A_x}{A_y\sin\phi}\right) - \arctan\left(\frac{A_y\cos\phi - \sqrt{3}A_x}{A_y\sin\phi}\right)\right]\right).\end{aligned} \tag{A6}$$

We are interested in the case of circular polarization where $A_x = A_y$ and $\phi = \frac{\pi}{2}$. The values of $\chi_{1,2,3}$ for circular polarization are given by $\chi_1 = \chi_2 = \chi_3 = \frac{iJ_n^2(\tilde{a}A)\sin\frac{2\pi n}{3}}{n\omega}$.

APPENDIX B: SLAVE-ROTOR MEAN FIELD TREATMENT OF THE OFF-RESONANT HAMILTONIAN

Within single site cluster mean field theory we can write the spinon-electron Hamiltonian $H_{fd} = \langle\Psi^\theta|H_{\text{eff}}^{\text{OR}}|\Psi^\theta\rangle$ and rotor Hamiltonian $H_\theta = \langle\Psi^{fd}|H_{\text{eff}}^{\text{OR}}|\Psi^{fd}\rangle$ as

$$\begin{aligned}H_{fd} = &\sum_{I,J,\beta,\sigma}\left(\langle\Psi^\theta|e^{-i\theta_{Ia}}|\Psi^\theta\rangle t_{I\alpha\sigma;J\beta\sigma}^{A,NN} f_{I\alpha\sigma}^\dagger d_{J\beta\sigma} + \text{H.c.}\right)\\ &+ \sum_{I,J,\sigma}\left(t_{Ib\sigma;Jc\sigma}^{A,NN} d_{Ib\sigma}^\dagger d_{Jc\sigma} + \text{H.c.}\right)\\ &+ \sum_{I,J,\alpha,\sigma}\left(t_{I\alpha\sigma;J\alpha\sigma}^{A,NNN} d_{I\alpha\sigma}^\dagger d_{J\alpha\sigma} + \text{H.c.}\right)\\ &+ U/2\sum_I \langle\Psi^\theta|n_{Ia}^\theta\left(n_{Ia}^\theta - 1\right)|\Psi^\theta\rangle - \mu_f N_f\end{aligned} \tag{B1}$$

$$\begin{aligned}H_\theta = &\sum_{I,J,\beta,\sigma}\left(t_{I\alpha\sigma;J\beta\sigma}^{A,NN}\langle\Psi^{fd}|f_{I\alpha\sigma}^\dagger d_{J\beta\sigma}|\Psi^{fd}\rangle e^{-i\theta_{Ia}} + \text{H.c.}\right)\\ &+ \sum_{I,J,\sigma}\langle\Psi^{fd}|\left(t_{Ib\sigma;Jc\sigma}^{A,NN} d_{Ib\sigma}^\dagger d_{Jc\sigma} + \text{H.c.}\right)|\Psi^{fd}\rangle\\ &+ \sum_{I,J,\alpha,\sigma}\langle\Psi^{fd}|\left(t_{I\alpha\sigma;J\alpha\sigma}^{A,NNN} d_{I\alpha\sigma}^\dagger d_{J\alpha\sigma} + \text{H.c.}\right)|\Psi^{fd}\rangle\\ &+ U/2\sum_I n_{Ia}^\theta\left(n_{I,a}^\theta - 1\right) - \mu_\theta N_\theta.\end{aligned} \tag{B2}$$

Here, $t_{I\alpha\sigma;J\beta\sigma}^{ANN}$ and $t_{I\alpha\sigma;J\alpha\sigma}^{ANNN}$ are the NN and NNN hopping amplitudes that were contained in $t_{I\alpha\sigma;J\beta\sigma}^{A}$ in $H_{\text{eff}}^{\text{OR}}$, in the main paper. In the first term of Eq. (B1), β runs over b and c. This term is the a-b and a-c, NN kinetic energy terms, where the bare t_{ab} and t_{ac} are renormalized by $\Phi_{Ia} = \langle\Psi^\theta|e^{-i\theta_{Ia}}|\Psi^\theta\rangle$. Within the mean field ansatz, Φ_{Ia} is assumed to be the same on all a sites. The second term is the bare kinetic term containing only b-c hopping. In the third term of Eq. (B1), the α summation goes over b and c and contains only t_{bb} and t_{cc} NNN hopping terms. This in because the emergent NNN

hopping amplitude t_{aa} is zero for our choice on bare hopping amplitudes, i.e.,$t_{ab} = t_{ac}$. We note that in H_{fd}, Φ_{Ia}, which is assumed to be the same on each a site, scales the NN hopping terms only. Thus when the local Mott transition occurs, the NN term in the Hamiltonian vanishes.

We start with a given Φ_{Ia}, assumed to be the same on all a sites within the single site rotor cluster mean field theory, and then diagonalize the spinon Hamiltonian. Now with the resultant eigenvectors and eigenvalues average Φ_{Ia} is calculated. The constraint equation, Eq. (11) in the main paper, is imposed at a mean field level, which reads as:

$$\langle n^{\theta}_{Ia}\rangle + \langle n^{f}_{Ia\uparrow}\rangle + \langle n^{f}_{Ia\downarrow}\rangle = 1. \tag{B3}$$

The average spinon occupation on the site a is identified to the electron occupation and the chemical potential μ_θ is adjusted to fix the rotor occupation so that it satisfies the mean field constraint equation. In our calculation, the Hilbert space for the interacting rotor Hamiltonian is restricted by limiting the local a site occupation to a maximum occupation of 3. Then Φ_{Ia} is used in H_{fd} and the spinon Hamiltonian is rediagonalized. The process is repeated until energy convergence is achieved.

1. DOS calculation

The main observable we focus on is the sublattice projected density of states (PDOS). The PDOS is defined in general as $N_\gamma(\omega) = \sum_{\alpha,\sigma}\sum_{i_\gamma}|\langle\chi_\alpha|i_\gamma,\sigma\rangle|^2\delta(\omega-\epsilon_\alpha)$, where $\gamma = a, b, c$ sites in the Ith unit cell. Here, $\{|\chi_\alpha\rangle\}$ and $\{\epsilon_\alpha\}$ correspond to the eigenvectors and eigenvalues of H. PDOS calculation is standard and is not repeated here. Below we focus on the PDOS for the interacting sublattice a. Since we have split the electron into a rotor and a spinon at every a site of our problem, we first need to reconstruct the (electron) single particle Green's function and then take its imaginary part to compute the spectral function and the PDOS. To do so, we begin with the local (on-site) retarded Matsubara Green's function at a site a in a unit cell I, which can be defined as,

$$\begin{aligned} G_{Ia\sigma}(i\omega_n) &= -\int_0^\beta d\tau e^{i\omega_n\tau}\langle\Psi|d_{Ia,\sigma}(\tau)d^\dagger_{Ia,\sigma}(0)|\Psi\rangle \\ &= -\int_0^\beta d\tau e^{i\omega_n\tau}\langle\Psi^{fd}|f_{I\alpha\sigma}(\tau)f^\dagger_{I\alpha\sigma}(0)|\Psi^{fd}\rangle \\ &\quad\times\langle\Psi^{\theta}|e^{-i\theta_{I\alpha}(\tau)}e^{i\theta_{I\alpha}(0)}|\Psi^{\theta}\rangle. \end{aligned} \tag{B4}$$

The above decomposition of electron Green's function into a convolution of rotor and spinon Green's functions is possible for the chosen mean field ansatz $|\Psi^{fd}\rangle|\Psi^{\theta}\rangle$. The spinon correlator in Eq. (B4) can be calculated as

$$\begin{aligned} &\frac{1}{2}\sum_\sigma\langle f_{I\alpha\sigma}(\tau)f^\dagger_{I\alpha\sigma}(0)\rangle \\ &= \frac{1}{2}\sum_{\alpha\sigma}\left|\langle\chi^f_\alpha|I\alpha,\sigma\rangle\right|^2\left[1-n_f\left(\epsilon^f_\alpha-\mu_f\right)\right]e^{-\tau(\epsilon^f_\alpha-\mu_f)}. \end{aligned} \tag{B5}$$

Here, $\{|\chi^f_\alpha\rangle\}$ and $\{\epsilon^f_\alpha\}$ are the spinon eigenvectors and eigenvalues, respectively. The rotor correlator in Eq. (B4) can be expressed as

$$\begin{aligned} &\langle e^{-i\theta_{I\alpha,\sigma}(\tau)}e^{i\theta_{I\alpha,\sigma}(0)}\rangle \\ &= \frac{1}{Z_\theta}\sum_{m,n}e^{-\beta\epsilon_m}\langle m|e^{-i\theta_{I\alpha,\sigma}}|n\rangle\langle n|e^{i\theta_{I\alpha,\sigma}}|m\rangle e^{\tau(\epsilon_m-\epsilon_n)}, \end{aligned} \tag{B6}$$

where $\{\epsilon_m\}$ and $\{|m\rangle\}$ are the eigenvalues and corresponding eigenvectors of the rotor Hamiltonian H_θ. Here, Z_θ is the rotor partition function defined as $\sum_m e^{-\beta\epsilon_m}$. Using Eq. (B4), the integration over imaginary time τ can be performed. We then analytically continue back to the real frequency to obtain $G_{I\alpha\sigma}(\omega)$. The PDOS is obtained from the corresponding imaginary part as usual.

APPENDIX C: CHERN NUMBERS AND EDGE MODE CALCULATIONS

The Chern number is defined for nth Bloch band as

$$C_n = \frac{1}{2\pi i}\int_T d^2kF_{ij}(k). \tag{C1}$$

The integration is over the full two-dimensional Brillouin zone. The Berry connection and associated curvature is defined as

$$A_i(k) = \langle n(k)|\partial_i|n(k)\rangle, \tag{C2}$$

$$F_{i,j} = \partial_iA_j - \partial_jA_i, \tag{C3}$$

where $n(k)$ is the normalized Bloch wave function of the nondegenerate nth Bloch band that is calculated by diagonalizing the momentum space Bloch Hamiltonian. For numerical calculation we employ the method discussed in Ref. [87].

To obtain a solution for the edge state, we have to consider a ribbon geometry. Here we adopt the periodic boundary condition along the x axis and along y we have an open boundary condition. Thus, k_x is a good quantum number here. Now performing the Fourier transformation only along the x direction, the problem is reduced to one dimensional (1D) having only k_x as the variable. Hence, the 1D Hamiltonian can be written as

$$H_{k_x} = \sum_{I,J,\alpha,\beta,\sigma}^{N} t^{A,k_x}_{I\alpha\sigma;J\beta\sigma}d^{k_x\dagger}_{I\alpha\sigma}d^{k_x}_{J\beta\sigma} + \text{H.c.}, \tag{C4}$$

where, I, J denote the site indices, N is the total number of lattice sites along the y direction, and α, β run oven a, b, and c. $t^{A,k_x}_{I\alpha\sigma;J\beta\sigma'}$ contains all the nearest and next nearest Fourier transformed hopping terms. Now diagonalizing the Hamiltonian numerically we obtain the required 1D edge spectra. In our case, for the edge calculation we consider $A = 1.5t$ and $N = 10$. Both the Chern number and the edge mode calculations are carried out for H_{fd}, once the SR-MFT results have converged.

APPENDIX D: TWO *A* SITE IN THE ROTOR CLUSTER

In the previous single site cluster calculation we take nearest neighbor hopping in such a way that light induced a-a next-nearest neighbor is vanished. Now we allow small

NNN a-a hopping by considering $t_{ab} \neq t_{ac}$. The corresponding spinon-electron and rotor Hamiltonians read as

$$H_{fd} \to H_{fd}^{\square} = H_{fd} + \sum_{I,J,\sigma} \left(\langle \Psi^{\theta} | e^{-i\theta_{Ia}} e^{i\theta_{Ja}} | \Psi^{\theta} \rangle t_{Ia\sigma;Ja\sigma}^{A,NNN} f_{Ia\sigma}^{\dagger} f_{Ja\sigma} + \text{H.c.} \right) \quad \text{(D1)}$$

$$H_{\theta} \to H_{\theta}^{\square} = H_{\theta} + \sum_{I,J,\sigma} \left(\langle \Psi^{fd} | f_{Ia\sigma}^{\dagger} f_{Ja\sigma} | \Psi^{fd} \rangle t_{Ia\sigma;Ja\sigma}^{A,NNN} e^{-i\theta_{Ia}} e^{i\theta_{Ja}} + \text{H.c.} \right). \quad \text{(D2)}$$

Here, $t_{Ia\sigma;Ja\sigma'}^{A,NNN}$ denotes the light driven direct a-a hopping amplitudes. This additional term in $H_{\theta}^{\square}$ is further decoupled in a kinetic term decoupling scheme $e^{-i\theta_{Ia}} e^{i\theta_{Ja}} \to \langle \Psi^{\theta} | e^{-i\theta_{Ia}} | \Psi^{\theta} \rangle e^{i\theta_{Ja}}$ or $\Phi_{Ia} e^{i\theta_{Ja}}$. Since Φ_{Ia} is assumed to be uniform, this implies that the additional term in $H_{\theta}^{\square}$ reduces to a local term. The solution of the four site cluster then proceeds exactly like the single site cluster case discussed in Appendix B, the difference being that a four site rotor Hamiltonian is diagonalized instead of a single site cluster. The four site (a-b-a-c) parallelogram cluster, indicated by the shaded parallelogram (enclosed within the dashed lines), is shown in Fig. 6(b). Also, as for the one site cluster, we allow local rotor occupation of 3 ion each a site in $H_{\theta}^{\square}$.

We note that in addition to $\langle \Psi^{\theta} | e^{-i\theta_{Ia}} | \Psi^{\theta} \rangle$ or Φ_{Ia} that renormalizes the NN hopping, $\langle \Psi^{\theta} | e^{-i\theta_{Ia}} e^{i\theta_{Ja}} | \Psi^{\theta} \rangle$ now scales the NNN hopping between the a sites. In the insulating phase when $\Phi_{Ia} = 0$, the rotor kinetic energy within the cluster $\langle \Psi^{\theta} | e^{-i\theta_{Ia}} e^{i\theta_{Ja}} | \Psi^{\theta} \rangle$ is not zero. It encodes the virtual charge fluctuations. In the insulating phase, the NN a-b and a-c hopping amplitudes are renormalized to zero (as $\Phi_{Ia} = 0$). In this regime NN t_{bc}, the NNN a-a, b-b, and c-c terms survive. When t_{aa} is chosen to be zero $H_{fd}^{\square}$ has the hopping connectivity of the Kane-Mele model. When $t_{aa} \neq 0$, the virtual charge fluctuations within the four site rotor cluster allow a a-a hopping mediated spinon kinetic energy contribution to the total kinetic energy in $H_{fd}^{\square}$. The resultant phase diagram is shown in Fig. 6(a). In Fig. 5(a), only the first band touching point was indicated by the red arrow. Here for completeness, for a specific value of nonzero t_{aa}, we show all the band touching points in the phase diagram [see Fig. 6(a)] as was shown for the $t_{aa} = 0$ case in Fig. 2(a). Comparison shows that these remain qualitatively unchanged, as is discussed in the subsection 4 in the main paper. In Fig. 6(c), the variation of all NNN hopping parameters are shown as a function of A for the bare parameters indicated in the figure.

[1] C. L. Kane and E. J. Mele, Phys. Rev. Lett. **95**, 226801 (2005).
[2] B. A. Bernevig, T. L. Hughes, and S.-C. Zhang, Science **314**, 1757 (2006).
[3] J. E. Moore, Nature (London) **464**, 194 (2010).
[4] X.-L. Qi and S.-C. Zhang, Rev. Mod. Phys. **83**, 1057 (2011).
[5] J. Maciejko, T. L. Hughes, and S.-C. Zhang, Annu. Rev. Condens. Matter Phys. **2**, 31 (2011).
[6] M. Z. Hasan and J. E. Moore, Annu. Rev. Condens. Matter Phys. **2**, 55 (2011).
[7] D. J. Thouless, M. Kohmoto, M. P. Nightingale, and M. den Nijs, Phys. Rev. Lett. **49**, 405 (1982).
[8] L. Fu and C. L. Kane, Phys. Rev. B **76**, 045302 (2007).
[9] J. C. Y. Teo, L. Fu, and C. L. Kane, Phys. Rev. B **78**, 045426 (2008).
[10] D. Pesin and A. H. MacDonald, Nat. Materials **11**, 409 (2012).
[11] C. Nayak, S. H. Simon, A. Stern, M. Freedman, and S. Das Sarma, Rev. Mod. Phys. **80**, 1083 (2008).
[12] M. Ezawa, New J. Phys. **14**, 033003 (2012).
[13] A. Stern and N. H. Linder, Science **339**, 1179 (2013).
[14] C. L. Kane and E. J. Mele, Phys. Rev. Lett. **95**, 146802 (2005).
[15] M. König, S. Wiedmann, C. Brüne, A. Roth, H. Buhmann, L. W. Molenkamp, X.-L. Qi, and S.-C. Zhang, Science **318**, 766 (2007).
[16] D. Culcer, Physica E **44**, 860 (2012).
[17] Y. Xia, D. Qian, D. Hsieh, L. Wray, A. Pal, H. Lin, A. Bansil, D. Grauer, Y. S. Hor, R. J. Cava *et al.*, Nat. Phys. **5**, 398 (2009).
[18] H. Zhang, C.-X. Liu, X.-L. Qi, X. Dai, Z. Fang, and S.-C. Zhang, Nat. Phys. **5**, 438 (2009).
[19] M. Z. Hasan and C. L. Kane, Rev. Mod. Phys. **82**, 3045 (2010).
[20] S. Rachel, Rep. Prog. Phys. **81**, 116501 (2018).
[21] S. Rachel and K. Le Hur, Phys. Rev. B **82**, 075106 (2010).
[22] S. Raghu, X.-L. Qi, C. Honerkamp, and S.-C. Zhang, Phys. Rev. Lett. **100**, 156401 (2008).
[23] D. Pesin and L. Balents, Nat. Phys. **6**, 376 (2010).
[24] M. Dzero, K. Sun, V. Galitski, and P. Coleman, Phys. Rev. Lett. **104**, 106408 (2010).
[25] M.-T. Tran, T. Takimoto, and K.-S. Kim, Phys. Rev. B **85**, 125128 (2012).
[26] S. Jana, A. Saha, and A. Mukherjee, Phys. Rev. B **100**, 045420 (2019).
[27] A. Shitade, H. Katsura, J. Kuneš, X.-L. Qi, S.-C. Zhang, and N. Nagaosa, Phys. Rev. Lett. **102**, 256403 (2009).
[28] S. Chadov, X. Qi, J. Kübler, G. H. Fecher, C. Felser, and S. C. Zhang, Nat. Mater. **9**, 541 (2010).
[29] H. Lin, L. A. Wray, Y. Xia, S. Xu, S. Jia, R. J. Cava, A. Bansil, and M. Z. Hasan, Nat. Mater. **9**, 546 (2010).
[30] T. Oka and H. Aoki, Phys. Rev. B **79**, 081406(R) (2009).
[31] N. H. Lindner, G. Refael, and V. Galitski, Nat. Phys. **7**, 490 (2011).
[32] B. Dóra, J. Cayssol, F. Simon, and R. Moessner, Phys. Rev. Lett. **108**, 056602 (2012).
[33] Y. Wang, H. Steinberg, P. Jarillo-Herrero, and N. Gedik, Science **342**, 453 (2013).
[34] M. C. Rechtsman, J. M. Zeuner, Y. Plotnik, Y. Lumer, D. Podolsky, F. Dreisow, S. Nolte, M. Segev, and A. Szameit, Nature (London) **496**, 196 (2013).
[35] G. Jotzu, M. Messer, R. Desbuquois, M. Lebrat, T. Uehlinger, D. Greif, and T. Esslinger, Nature (London) **515**, 237 (2014).
[36] Y.-G. Peng, C.-Z. Qin, D.-G. Zhao, Y.-X. Shen, X.-Y. Xu, M. Bao, H. Jia, and X.-F. Zhu, Nat. Commun. **7**, 13368 (2016).

[37] L. Jiang, T. Kitagawa, J. Alicea, A. R. Akhmerov, D. Pekker, G. Refael, J. I. Cirac, E. Demler, M. D. Lukin, and P. Zoller, Phys. Rev. Lett. **106**, 220402 (2011).

[38] A. Kundu and B. Seradjeh, Phys. Rev. Lett. **111**, 136402 (2013).

[39] P. M. Perez-Piskunow, G. Usaj, C. A. Balseiro, and L. E. F. Foa Torres, Phys. Rev. B **89**, 121401(R) (2014).

[40] Z. Gu, H. A. Fertig, D. P. Arovas, and A. Auerbach, Phys. Rev. Lett. **107**, 216601 (2011).

[41] A. Kundu, H. A. Fertig, and B. Seradjeh, Phys. Rev. Lett. **113**, 236803 (2014).

[42] A. Farrell and T. Pereg-Barnea, Phys. Rev. Lett. **115**, 106403 (2015).

[43] H. Sambe, Phys. Rev. A **7**, 2203 (1973).

[44] J. Klinovaja, P. Stano, and D. Loss, Phys. Rev. Lett. **116**, 176401 (2016).

[45] P. Titum, N. H. Lindner, M. C. Rechtsman, and G. Refael, Phys. Rev. Lett. **114**, 056801 (2015).

[46] T. Kitagawa, T. Oka, A. Brataas, L. Fu, and E. Demler, Phys. Rev. B **84**, 235108 (2011).

[47] G. Usaj, P. M. Perez-Piskunow, L. E. F. FoaTorres, and C. A. Balseiro, Phys. Rev. B **90**, 115423 (2014).

[48] M. Ezawa, Phys. Rev. Lett. **110**, 026603 (2013).

[49] N. D. Drummond, V. Zolyomi, and V. I. Fal'Ko, Phys. Rev. B **85**, 075423 (2012).

[50] C.-C. Liu, W. Feng, and Y. Yao, Phys. Rev. Lett. **107**, 076802 (2011).

[51] P. Mohan, R. Saxena, A. Kundu, and S. Rao, Phys. Rev. B **94**, 235419 (2016).

[52] K. Saha, Phys. Rev. B **94**, 081103(R) (2016).

[53] SK. Firoz Islam and A. Saha, Phys. Rev. B **98**, 235424 (2018).

[54] A. Agarwala and D. Sen, Phys. Rev. B **95**, 014305 (2017).

[55] K. Hejazi, J. Liu, and L. Balents, Phys. Rev. B **99**, 205111 (2019).

[56] M. Messer, K. Sandholzer, F. Görg, J. Minguzzi, R. Desbuquois, and T. Esslinger, Phys. Rev. Lett. **121**, 233603 (2018).

[57] K. Takasan, M. Nakagawa, and N. Kawakami, Phys. Rev. B **96**, 115120 (2017).

[58] L. D'Alessio and M. Rigol, Phys. Rev. X **4**, 041048 (2014).

[59] L. W. Clark, L.-C. Ha, C.-Y. Xu, and C. Chin, Phys. Rev. Lett. **115**, 155301 (2015).

[60] T. Iadecola, L. H. Santos, and C. Chamon, Phys. Rev. B **92**, 125107 (2015).

[61] A. Rapp, X. Deng, and L. Santos, Phys. Rev. Lett. **109**, 203005 (2012).

[62] J. Gong, L. Morales-Molina, and P. Hänggi, Phys. Rev. Lett. **103**, 133002 (2009).

[63] D. A. Abanin, W. De Roeck, and F. Huveneers, Phys. Rev. Lett. **115**, 256803 (2015).

[64] D. Abanin, W. De Roeck, W. W. Ho, and F. Huveneers, Commun. Math. Phys. **354**, 809 (2017).

[65] A. Lazarides, A. Das, and R. Moessner, Phys. Rev. E **90**, 012110 (2014).

[66] These arguments for global driving of the system are based on Lieb-Robinson bounds discussed in Commun. Math. Phys. **28**, 251 (1972), and their generalizations detailed in Contemporary Mathematics **529**, 202 (2010), that hold for systems with short range interactions, gapped ground states, and decaying correlation functions. The Mott state within the Hubbard model has been investigated recently in this limit in Phys. Rev. Lett. **121**, 233603 (2018). In this spirit we choose a $(\Omega \gg U, t)$, which allows for a large regime in time before thermalization happens.

[67] I. Huvac and S. Wilson, Brillouin-Wigner Methods for Many-Body Systems (Springer, Dordrecht, Heidelberg, 2010).

[68] In the off resonant modulation, the frequency of external driving is the dominant energy scale, such that $(\Omega \gg U, t)$, this allows us to safely neglect the exchange of real photons as can happen when $U \sim \Omega$. This allows us to work with an effective Hamiltonian with renormalized bare hopping, emergent NNN hopping elements and the bare Hubbard U. The analysis of the validity of the Off resonant condition has been carried out in Phys. Rev. Lett. **121**, 233603 (2018).

[69] Strictly speaking all bands in the off-resonant driven system are quasienergy bands in the Floquet spectrum. However for brevity we will simply refer to them as bands in the paper. Similarly, the ground states mentioned in the paper are lowest energy states in the quasi energy spectra.

[70] S. Florens and A. Georges, Phys. Rev. B **70**, 035114 (2004).

[71] E. Zhao and A. Paramekanti, Phys. Rev. B **76**, 195101 (2007).

[72] T. Mikami, S. Kitamura, K. Yasuda, N. Tsuji, T. Oka, and H. Aoki, Phys. Rev. B **93**, 144307 (2016).

[73] E. S. Mananga and T. Charpentier, The Journal of Chemical Physics **135**, 044109 (2011).

[74] S. Blanes, F. Casas, J. Oteo, and J. Ros, Phys. Rep. **470**, 151 (2009).

[75] A. Eckardt and E. Anisimovas, New J. Phys. **17**, 093039 (2015).

[76] M. Bukov, L. D'Alessio, and A. Polkovnikov, Adv. Phys. **64**, 139 (2015).

[77] J. H. Shirley, Phys. Rev. **138**, B979 (1965).

[78] B. Keimer, S. A. Kivelson, M. R. Norman, S. Uchida, and J. Zaanen, arXiv:1409.4673 (2014).

[79] B. Lau and A. J. Millis, Phys. Rev. Lett. **110**, 126404 (2013).

[80] We note that the trapped charges at the a sublattice form quantum local moments. In the present paper however our modest aim is to focus on the physics of charge fluctuations, and we do not consider the possibility of Kondo screening or RKKY mediated magnetic order.

[81] C. Becker, P. Soltan-Panahi, J. Kronjäger, S. Dörscher, K. Bongs, and K. Sengstock, New J. Phys. **12**, 065025 (2010).

[82] R. Jördens, N. Strohmaier, K. Günter, H. Moritz, and T. Esslinger, Nature (London) **455**, 204 (2008).

[83] H. Lignier, C. Sias, D. Ciampini, Y. Singh, A. Zenesini, O. Morsch, and E. Arimondo, Phys. Rev. Lett. **99**, 220403 (2007).

[84] R. Qi and H. Zhai, Phys. Rev. Lett. **106**, 163201 (2011).

[85] C. Chin, R. Grimm, P. Julienne, and E. Tiesinga, Rev. Mod. Phys. **82**, 1225 (2010).

[86] R. Yamazaki, S. Taie, S. Sugawa, and Y. Takahashi, Phys. Rev. Lett. **105**, 050405 (2010).

[87] T. Fukui, Y. Hatsugai, and H. Suzuki, J. Phys. Soc. Jpn. **74**, 1674 (2005).